

Automatic Bone Segmentation and Alignment From MR Knee Images

Liang Shan^a, Christopher Zach^a, Martin Styner^a, Cecil Charles^b, Marc Niethammer^a

^aDepartment of Computer Science, UNC Chapel Hill, Chapel Hill, NC 27599, USA;

^bDepartment of Radiology, Duke University, Durham, NC 27705, USA

ABSTRACT

Automatic image analysis of magnetic resonance (MR) images of the knee is simplified by bringing the knee into a reference position. While the knee is typically put into a reference position during image acquisition, this alignment will generally not be perfect. To correct for imperfections, we propose a two-step process of bone segmentation followed by elastic tissue deformation.

The approach makes use of a fully-automatic segmentation of femur and tibia from T1 and T2* images. The segmentation algorithm is based on a continuous convex optimization problem, incorporating regional, and shape information. The regional terms are included from a probabilistic viewpoint, which readily allows the inclusion of shape information. Segmentation of the outer boundary of the cortical bone is encouraged by adding simple appearance-based information to the optimization problem. The resulting segmentation without the shape alignment step is globally optimal.

Standard registration is problematic for knee alignment due to the distinct physical properties of the tissues constituting the knee (bone, muscle, etc.). We therefore develop an alternative alignment approach based on a simple elastic deformation model combined with strict enforcement of similarity transforms for femur and tibia based on the obtained segmentations.

Keywords: fully-automatic, segmentation, region information, appearance information, globally optimal, shape model, alignment, registration

1. INTRODUCTION

Osteoarthritis (OA) is one of the major causes of long-term disability affecting millions of people. Cartilage loss¹ is believed to be the dominating factor in OA and hip and knee involvement are most common. Magnetic resonance imaging (MRI) can evaluate the loss of cartilage and is increasingly accepted as a primary method to evaluate progression of OA^{2,3,4}. Automatic or semi-automatic analysis of knee images is desirable for example to quantify cartilage loss. Accurate knee alignment, as discussed in this paper, can be a beneficial pre-processing step for such analysis.

Many methods have been applied to bone and cartilage segmentation, e.g., region growing approaches⁵, medial models, active shape models⁶, general deformable models (such as live-wire, active contour or active surface models)⁷, clustering methods⁸, and graph-based approaches⁹. However most of these methods require user interaction to place seeds or identify landmarks. Further, the resulting object segmentation may strongly depend on the initialization of the model, since the underlying optimization problems are typically non-convex and therefore prone to result in sub-optimal solutions. Classical formulations for curve and surface evolution as well as active shape model fall into this class of non-convex optimization problems.

Graph-based approaches (graph-cuts) have been highly successful to obtain globally optimal solutions for a class of discrete optimization problems. They have also been used to segment cartilage^{9,10}. However, large data volumes require the construction of large graphs (in particular, when metrication errors are to be minimized) and parallel implementations are not straightforward¹¹. Continuous versions of graph-cuts have recently been proposed¹², but have so far not been used in the context of OA. These new methods can be efficiently implemented,

Email: shan@cs.unc.edu.

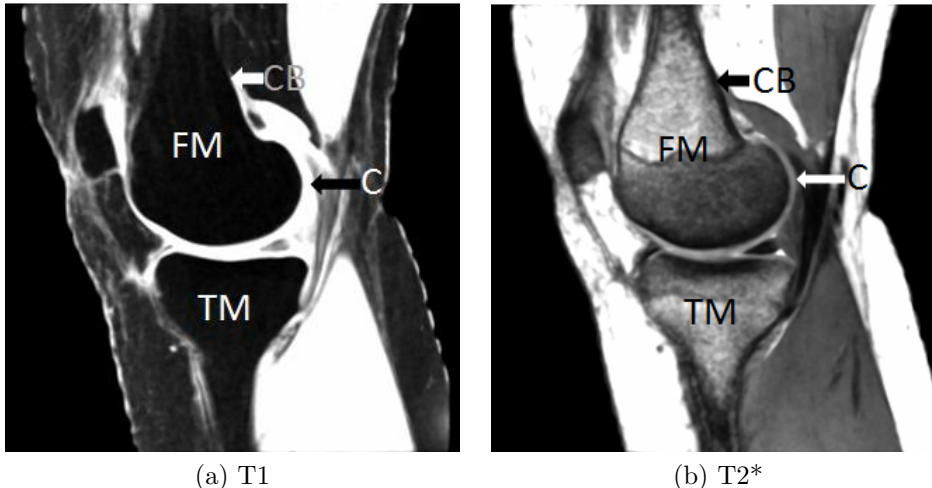


Figure 1. Sample sagittal slices from T1 and T2* knee MR images. FM: trabecular bone, femur, containing bone marrow. TM: trabecular bone, tibia, containing bone marrow. C: Cartilage. CB: cortical bone.

do not exhibit metrication artifacts and result in globally optimal solutions. We will extend the continuous graph cut formulation for our segmentation of femur and tibia, to take advantage of these attractive properties.

To analyze knee images across subjects and time, an accurate alignment of the images is desired but is frequently not achieved during image acquisition. Since the tissues (bone, muscle, etc.) constituting the knee have different physical properties and the knee joints may have different angular positioning, the standard image-based globally affine registration is not well suited for the alignment of knee images. We therefore develop an alternative segmentation-based alignment approach which can deform bones rigidly and surrounding tissue elastically.

Section 2 discusses the segmentation approach. The inclusion of shape information is discussed in Section 3. Section 4 introduces a physically reasonable registration scheme to bring the knee into a reference configuration. Results are shown in Section 5. The paper concludes with a summary and future work.

2. SEGMENTATION

The proposed segmentation algorithm makes use of the following properties for the T1 and the T2* knee MR images as related to the appearance of bone and surrounding tissue (see Figure 1 for an illustration):

- T1: Bone marrow and cortical bone appear dark. Cartilage appears bright, tissue dark gray or bright.
- T2*: Bone marrow appears bright. Cortical bone appears dark. Tissue is dark gray or bright.

Segmenting femur and tibia from a T1 image alone is challenging, due to partially insufficient delineation between bone and surrounding tissue. Segmentation from a T2* image is complicated by insufficient image contrast close to the knee joint. We thus use the T1 and the T2* image jointly, to simplify the segmentation.

Chan-Vese segmentation¹³ aims at finding an optimal image partition into a uniform foreground and background region. It is classically formulated as a curve/surface-based optimization problem of the form

$$E(c_1, c_2, C) = Length(C) + \lambda_1 \int_{inside(C)} (c_1 - I(x))^2 dx + \lambda_2 \int_{outside(C)} (c_2 - I(x))^2 dx \quad (1)$$

where $I(\cdot)$ denotes image intensities, c_1 and c_2 are the intensity estimates for the interior and the exterior of the curve C (their means). This is a non-convex optimization problem, which complicates the solution. In particular, the obtained solution may only be a local optimum of the optimization problem.

In recent work by Appleton et al.¹² and Bresson et al.¹⁴ the optimization problems for conformal active contours and Chan-Vese segmentation have been recast as convex optimization problems, by formulating the

problem with respect to a labeling (indicator) function for foreground and background rather than with respect to a boundary curve/surface.

Specifically, Bresson et al.¹⁴ proposed the following convex functional for Chan-Vese segmentation:

$$E(u) = \int_{\Omega} g \|\nabla u\| d\Omega + \lambda \int_{\Omega} \overbrace{((c_1 - I(x))^2 - (c_2 - I(x))^2)}^r u d\Omega, \quad u \in [0, 1], \quad (2)$$

where u is an essentially binary labeling function, indicating foreground (1) and background (0), and g is an edge-indicator function, small at edges and large in uniform regions, Ω is the full image domain.

Our segmentation approach builds upon Equation 2. The region-based term r can be reformulated in a probabilistic way. We replace r by $\log \frac{P_i}{P_o}$, P_i and P_o probabilities of a pixel belonging to foreground and background respectively (where equal Gaussian probability distributions result in the Chan-Vese energy). A feature vector field (flux) \mathbf{F} is added to favor boundaries which have inward normal directions (pointing to the interior of the segmentation) aligned with \mathbf{F} . Thus, the overall optimization problem is to minimize the following convex energy functional

$$E(u) = \int_{\Omega} g \|\nabla u\| + ru + \mathbf{F} \cdot \nabla u d\Omega, \quad r = \log \frac{P_o}{P_i}. \quad (3)$$

A solution for u is obtained by the equivalent minimax problem

$$u^*, \mathbf{p}^* = \arg \left(\min_{u: u \in [0, 1]} \max_{\mathbf{p}: \|\mathbf{p}\| \leq g} \int_{\Omega} \mathbf{p} \cdot \nabla u + (r - \operatorname{div}(\mathbf{F}))u d\Omega \right), \quad r = \log \frac{P_o}{P_i}. \quad (4)$$

Here, the dual variable \mathbf{p} was introduced to rewrite the total variation term, incorporating the edge weight g . The divergence term is the result of integration by parts for the term $\mathbf{F} \cdot \nabla u$.

Computing the variation of the energy of Equation 4 yields the gradient descent/ascent scheme

$$u_t = -\nabla_u E = \operatorname{div}(\mathbf{p} + \mathbf{F}) - r, \quad \mathbf{p}_t = \nabla_{\mathbf{p}} E = \nabla u, \quad u \in [0, 1], \quad \|\mathbf{p}\| \leq g.$$

For the bone segmentation, we set $g = 1$ and

$$P_i = P(\text{bone} | I_{T_1}, I_{T_2}) = \frac{p(I_{T_1}, I_{T_2} | \text{bone})P(\text{bone})}{p(I_{T_1}, I_{T_2})}, \quad P_o = 1 - P_i,$$

where the likelihood $p(I_{T_1}, I_{T_2} | \text{bone})$ is computed from the joint histogram for I_{T_1} and I_{T_2} through Parzen windowing*. In the absence of spatial information $P(\text{bone}) = \frac{1}{2}$. We add shape information through alignment of a shape model (a shape atlas) to the essentially binary segmentation u , resulting in a spatially varying prior for $P(\text{bone})$ (see Section 3). To favor segmentation boundaries at image intensity transitions from dark to bright (moving towards the outside of the bone), we set $\mathbf{F} = \beta(\nabla I_{T_1} + \nabla I_{T_2})$, $\beta \in \mathbb{R}^+$. Favoring reverse transitions, would simply amount to $\beta \in \mathbb{R}^-$.

To demonstrate this effect, Figure 2 shows synthetic results for segmentations with desired intensity transitions. Since the regularizing term $g \|\nabla u\|$ favors short contours or small surfaces, the segmentation in Figure 2(b) only includes the white object in the center. The inclusion of the outer white object in Figure 2(c) is a direct result of the divergence term $\operatorname{div}(\mathbf{F}) \cdot u$, an equivalent form of $\mathbf{F} \cdot \nabla u$, which constitutes a region term at image edges. (See the approach in¹⁶ for a way to include such information without creating additional source/sink terms.) By reversing the flux term, opposite intensity transitions can be favored for the segmentation as shown in Figure 2(d). An overview of the segmentation algorithm is given in Figure 5.

*Prior to the computation of the histograms, we first mask out the image background followed by MR bias field correction using the MNI's N3 algorithm¹⁵. We also adjust intensity levels if needed.

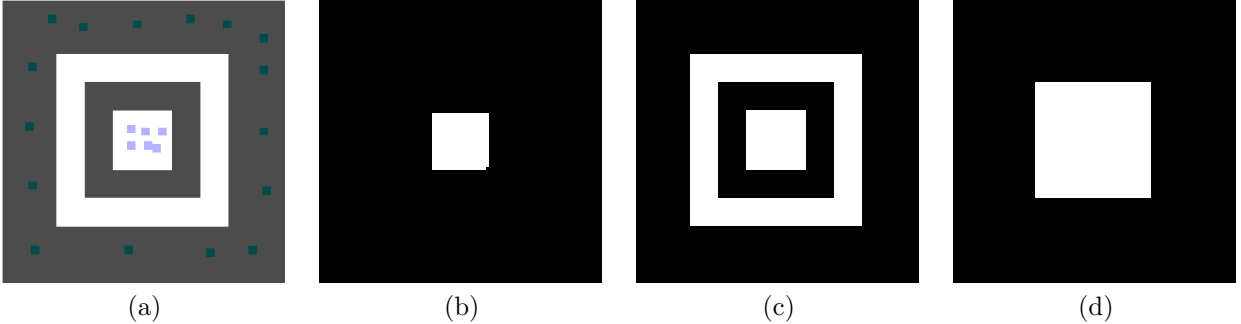


Figure 2. Segmentation results based on image (a) and its foreground (purple) and background (green) seedpoints, obtained by minimizing Equation (3) for $r = 0$ and $g = \frac{1}{1+\alpha\|\nabla I\|^p} + \epsilon$, vary based on \mathbf{F} . $\mathbf{F} = 0$ results in the standard edge-based segmentation, segmenting the image interior (b). Favoring bright-to-dark transitions through \mathbf{F} , segments both white objects (c). Favoring dark-to-bright transitions results in (d), which we will use to encourage segmentations at the outer boundary of the cortical bone.

3. REGISTRATION OF THE SHAPE MODEL

To introduce shape information, we alternately determine the segmentation u by solving Equation (4) and realigning the shape model. The shape model is simply a smoothed version of a binary segmentation mask from a reference case by user-adjusted segmentation. The shape mask was scaled to $[0.05, 0.85]$ followed by smoothing (so not to enforce the shape model strictly). A more sophisticated multi-channel shape model (e.g. together with intensities of the bone from T1 and T2* images), can also be used if necessary.

The shape model alignment is achieved by minimizing

$$E(\Phi_1, \Phi_2) = \int_{\Omega} \left(u - \sum_{i=1}^2 H_{\epsilon} \left(S_i \circ \Phi_i - \frac{1}{2} \right) \right)^2 + \prod_{i=1}^2 S_i \circ \Phi_i \, d\Omega. \quad (5)$$

Here, S_1 and S_2 are shape models (images) for femur and tibia respectively ($S_i : \Omega \mapsto [0, 1]$). Φ_1, Φ_2 correspond to similarity transforms in our implementation (though other transformation models could be used), H_{ϵ} is the smoothed Heaviside function. The first term aligns the shape model with the current segmentation u , whereas the second term discourages overlap between the two separate shape models S_1 and S_2 . After convergence, we compute the updated spatial prior as $P_{bone} = \max(S_1 \circ \Phi_1, S_2 \circ \Phi_2)$ and re-solve the segmentation problem 4. See Figure 3 for an illustration.

4. ALIGNMENT OF THE KNEE MR IMAGES

Once the segmentations for femur and tibia have been obtained, they can be aligned to reference bones (e.g., of an atlas image) to facilitate subsequent analysis and to infer deformations of the surrounding tissues. Transformation models between bone and surrounding tissue are typically distinct. Bones deform rigidly within-subject. Across subjects affine or similarity transforms are reasonable deformation assumptions. We choose a similarity transform to preserve bone shape. A variety of approaches exist to combine separate space transformations into one globally valid transformation, but only few enforce a desired local transformation exactly. Little et al.¹⁷ propose an alignment approach based on landmarks and regions which move rigidly. More generally, Haber et al.¹⁸ propose a registration framework based on constrained optimization, which can incorporate local transformation constraints, such as rigid motions. Our approach to enforce local transformation exactly is currently purely geometric. It is related to the approach by Haber et al.,¹⁸ but performs a simplified registration by using a registration of the obtained segmentations of femur and tibia and combining it with what is essentially a smoothing step.

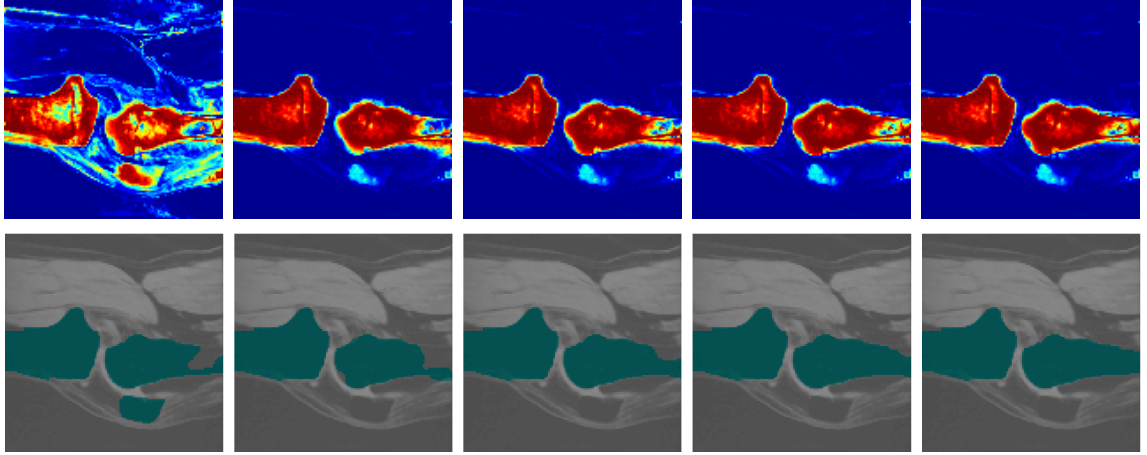


Figure 3. Evolution of bone probabilities (top) and resulting segmentation (bottom). Left: segmentation and probabilities do not use any shape information. Shape information is incorporated in subsequent segmentations. The shape model suppresses the patella and fills in areas that cannot be unambiguously identified based on image intensities.

To infer a smooth deformation of the tissue surrounding the bones, we minimize the elastic energy potential¹⁹

$$E(q) = \int_{\Omega} \frac{\mu}{4} \sum_{i,j=1}^3 \left(\frac{\partial q_j}{\partial x_i} + \frac{\partial q_i}{\partial x_j} \right)^2 + \frac{\lambda}{2} (\text{div} q)^2 d\Omega, \quad q = q_0 \in \Omega_b, \quad (6)$$

where q denotes the sought for displacement and q_0 is the known displacement for the bones defined on the transformed bone space, Ω_b ; λ and μ are the Lamé constants; μ is the shear modulus, specifying a material's resistance to shear movements. Upon minimization of (6) the overall space transformation is given as, $\Phi(x) = x + q$, mapping the untransformed to the transformed image. The variation of Equation 6 yields the gradient descent for the regularity term of elastic registration restricted to the domain $\Omega \setminus \Omega_b$:

$$q_{\theta} = -\nabla_q E(q) = \mu \Delta q + (\lambda + \mu) \nabla (\text{div} q), \quad q = q_0 \in \Omega_b.$$

A materials reaction to compression or dilation is described by Poisson's ratio

$$\nu = \frac{\lambda}{2\mu + (d-1)\lambda}, \quad 2D : \nu \in [-1, 1], \quad 3D : \nu \in [-1, \frac{1}{2}].$$

Materials with $\nu > 0$ contract (expand) orthogonally to the direction of expansion (compression). Materials with $\nu = 0$ do not change shape orthogonally to the direction of change. Since our primary objective is a faithful geometry close to the knee joint, we pick $\nu > 0$, but smaller than the upper bound for ν , which describes rubber-like materials.

Of note, for the alignment of the knee, a smooth space transformation is a simplifying assumption. Strictly speaking the transformation would need to support sliding motions, which happens when cartilage slides with respect to each other upon knee movement. Figure 4 illustrates the simplified behavior for a set of stylized bones for a range of Poisson ratios. The geometric alignment obtained can be used as an initial image normalization (just as deformable registration is frequently preceded by affine registration in brain imaging for example), but should ultimately be combined with image information in a registration framework accounting for local sliding motions and the elasticity differences in cartilage and surrounding tissue.

5. RESULTS

We demonstrate the behavior of the segmentation on a synthetic case and of the complete proposed segmentation algorithm on real MR images (T1 weighted 3D SPGR and T2* 3D GRE images acquired sagittally at a resolution

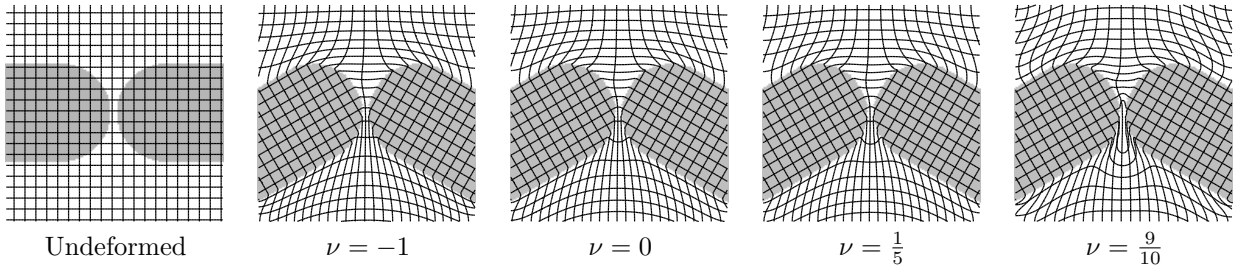


Figure 4. Two-dimensional example: Elastic alignment for a set of Poisson ratios ($\nu \in [-1, 1]$ in 2D). Material becomes rubber-like for $\nu \rightarrow 1$. $\nu = -1$ results in the minimization of the Dirichlet energy (i.e., $\mu = -\lambda > 0$) in 2D.

Algorithm 1: Bone segmentation

Data: T1, T2* images; shape model; model of image likelihoods
Result: Bone segmentation
Mask out image background ;
Perform MRI bias field correction using MNI’s N3 algorithm¹⁵ ;
Smooth images after bias field correction ;
Adjust image intensity levels to reference levels ;
Align shape model to likelihood image ;
Perform segmentation ;
repeat
| Align shape model to segmentation ;
| Perform segmentation with aligned shape model ;
until *convergence* ;

Figure 5. Bone segmentation pipeline.

of $0.29 \times 0.29 \times 1.5 \text{ mm}^3$ at 3T). Preliminary results were obtained on images downsampled to an approximately isotropic resolution of $1.17 \times 1.17 \times 1.5 \text{ mm}^3$.

Figure 6 shows the improvement achieved by including appearance information. Incorporating the desired intensity transitions allows for a simple combination of T1 and T2* edge terms, resulting in a good segmentation close to the knee joint (where the T1 image carries the best information) as well as for the remainder of the bone (where the T2* image is more reliable). Note the good agreement with the expert-obtained manual segmentation.

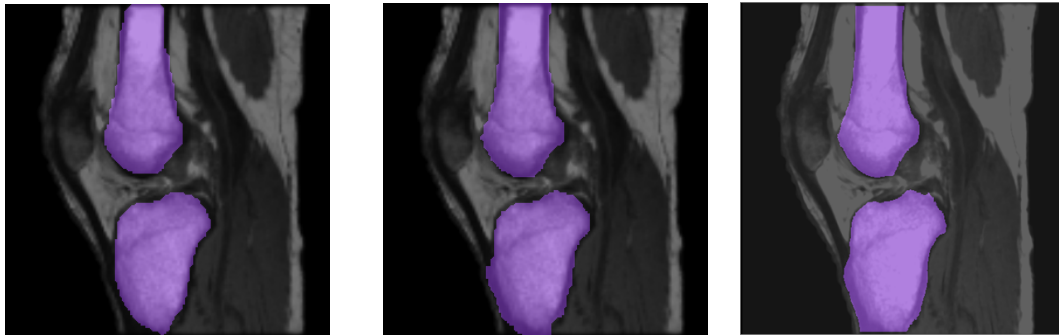
Figure 7 shows a sample segmentation of femur and tibia obtained after five iterations of segmentation and shape-model alignment. Both bones are segmented well. The cortical bone is also well captured. The shape model accounts for deficiencies of the region-based terms which are purely based on image-intensity and discards objects which are not of interest (such as the patella; compare also to Figure 3).

The bone-based alignment method improves the alignment significantly over the globally affine registration (see Figure 8). Not only the alignment of bones is improved, but also that of surrounding tissue.

6. CONCLUSION AND FUTURE WORK

The proposed segmentation approach has a number of advantages: (i) The segmentation step by itself (without shape model or given an aligned shape model) is globally optimal. It is thus not subject to local minima as is for example the case for classical curve or surface evolutions. (ii) The approach is fully-automatic. User-input is not required, but could easily be integrated if desired. (iii) Using a simple intensity-based appearance model for expected edge transitions, allows for an easy combination of edge-based information from both T1 and T2* images, while capturing the desired outer boundary of the cortical bone.

Future work will focus on the validation of the segmentation method with respect to manual segmentations. Further, we will explore a three-label (femur/tibia/background) segmentation formulation to ensure the separation of femur and tibia in case femur and tibia appear touching in the image. We will also focus on the



(a) without appearance term \mathbf{F} (b) with appearance term \mathbf{F} (c) ground truth
 Figure 6. Segmentations with and without appearance information overlaid onto the original T2* image.

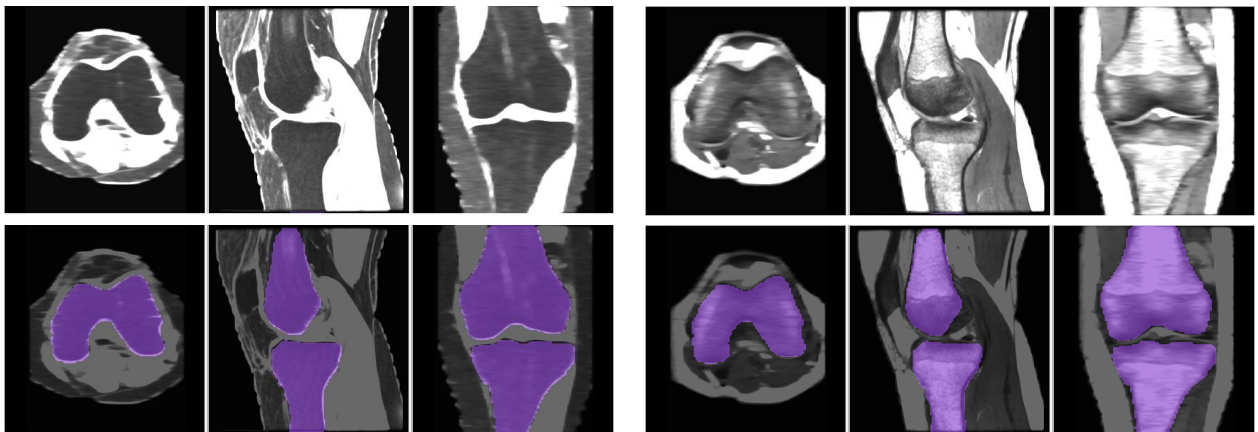


Figure 7. Top: Original images. Left T1 weighted, right T2* weighted. Bottom: Segmentation results overlaid onto the images. The segmentation captures the femur and tibia, while favoring the desired intensity transitions. This effect is particularly pronounced in the knee joint area.

realignment step: (i) On a refined modeling of the distinct material properties of tissues in the knee and (ii) on the modeling of transformations, which are not smooth, allow for local sliding of space, and incorporate image information for their estimation.

REFERENCES

- [1] Felson, D. T. and et al., “Osteoarthritis: New insights, part 1: The disease and risk factors,” *Annals of Internal Medicine* **133**, 635–646 (2000).
- [2] Raynauld, J. P., “Quantitative magnetic resonance imaging of articular cartilage in knee osteoarthritis,” *Current Opinions in Rheumatology* **15**(5), 647–650 (2003).
- [3] Cicuttini, F., Hankin, J., Jones, G., and Wluka, A., “Comparison of conventional standing knee radiographs and magnetic resonance imaging in assessing progression of tibiofemoral joint osteoarthritis,” *Osteoarthritis Cartilage* **13**, 722–727 (2005).
- [4] Raynauld, J. P., Martel-Pelletier, J., Berthiaume, M. J., and et al., “Quantitative magnetic resonance imaging evaluation of knee osteoarthritis progression over two years and correlation with clinical symptoms and radiologic changes,” *Arthritis Rheumatology* **50**(2), 476–487 (2004).
- [5] Tamez-Pena, J. G., Totterman, S., and Parker, K. J., “Unsupervised statistical segmentation of multispectral volumetric MR images,” *Proceedings of the SPIE Conference on Image Processing* **3661**, 300–311 (1999).
- [6] Frupp, J., Crozier, S., Warfield, S. K., and Ourselin, S., “Automatic segmentation of bone and extraction of the bone-cartilage interface from magnetic resonance images of the knee,” *Physics in Medicine and Biology* **52**, 1617–1631 (2007).



No registration.

Globally affine.

Elastic + similarity (bones).

Figure 8. Enforcing similarity transformations for femur and tibia and elastically transforming otherwise, results in an improved alignment over globally affine registration.

- [7] Brem, M. H., Brem, M. H., Lang, P. K., Neumann, G., Schlechtweg, P. M., Schneider, E., Jackson, R., Yu, J., Eaton, C. B., Hennig, F. F., Yoshioka, H., Pappas, G., and Duryea, J., “Magnetic resonance image segmentation using semi-automated software for quantification of knee articular cartilage - initial evaluation of a technique for paired scans,” *Skeletal Radiology* **28**(5), 505–511 (2009).
- [8] Folkesson, J., Dam, E. B., Olsen, O. F., Pettersen, P. C., and Christiansen, C., “Segmenting articular cartilage automatically using a voxel classification approach,” *IEEE Transactions on Medical Imaging* **26**(1), 106–115 (2007).
- [9] Shim, H., Chang, S., Tao, C., Wang, J.-H., Kwoh, C. K., and Bae, K. T., “Knee cartilage: Efficient and reproducible segmentation on high-spatial-resolution MR images with the semiautomated graph-cut method,” *Radiology* **251**(2), 548–556 (2009).
- [10] Bae, K. T., Shim, H., Tao, C., Chang, S., Wang, J. H., Boudreau, R., and Kwoh, C. K., “Intra- and inter-observer reproducibility of volume measurement of knee cartilage segmented from the oai mr image set using a novel semi-automated segmentation method,” *Osteoarthritis Cartilage* **17**, 1589–1597 (2009).
- [11] Delong, A. and Boykov, Y., “A scalable graph-cut algorithm for N-D grids,” in [*Proceedings of the Conference on Computer Vision and Pattern Recognition (CVPR)*], (2008).
- [12] Appleton, B. and Talbot, H., “Globally minimal surfaces by continuous maximal flows,” *IEEE Transactions on Pattern Analysis and Machine Intelligence* **28**(1), 106–118 (2006).
- [13] Chan, T. F. and Vese, L. A., “Active contours without edges,” *IEEE Transactions on Image Processing* **10**, 266–277 (2001).
- [14] Bresson, X., Esedoglu, S., Vandergheynst, P., Thiran, J.-P., and Osher, S., “Fast global minimization of the active contour/snake model,” *Journal of Mathematical Imaging and Vision* **28**, 151–167 (2007).
- [15] Sled, J. G., Zijdenbos, A. P., and Evans, A. C., “A non-parametric method for automatic correction of intensity non-uniformity in MRI data,” *IEEE Transactions on Medical Imaging* **17**, 87–97 (1998).
- [16] Zach, C., Shan, L., and Niethammer, M., “Globally optimal Finsler active contours,” in [*Proceedings of the 31st DAGM Symposium on Pattern Recognition*], 552–561 (2009).
- [17] Little, J. A., Hill, D. L. G., and Hawkes, D. J., “Deformations incorporating rigid structures,” in [*Proceedings of MMBIA*], 104–113 (1996).
- [18] Haber, E., Heldmann, S., and Modersitzki, J., “A framework for image-based constrained registration with an application to local rigidity,” tech. rep. (2009).
- [19] Modersitzki, J., [*Numerical Methods for Image Registration*], Oxford Science Publications (2004).